Toward High-Performing Topological Edge-State Optical Isolators

Dolendra Karki, Ramy El-Ganainy, and Miguel Levy*
Department of Physics and Henes Center for Quantum Phenomena, Michigan Technological University, Houghton, Michigan 49931, USA

(Received 5 October 2018; revised manuscript received 29 December 2018; published 19 March 2019)

We report on the experimental implementation of topological edge-state arrays with power confinement in the edge state as high as 29 dB relative to its farthermost channel. Average insertion losses of <2 dB in the edge channel vs total output power in the whole array are measured. The device follows a Su-Shrieffer-Heeger construction, consisting of seven waveguides fabricated on (100) liquid-phase-epitaxy-grown bismuth-substituted lutetium iron garnet films on a gadolinium gallium garnet substrate. The delocalization of the field can be realized by magnetizing only the single edge-state channel, thereby diverting the backscattered signal to serve as a high-performing optical isolator with a predicted isolation ratio as high as -50 dB. We discuss methods and challenges for full experimental implementation of a SSH topology-based optical isolator.

DOI: 10.1103/PhysRevApplied.11.034045

I. INTRODUCTION

The development of on-chip optical isolators for integrated photonic circuits has been actively pursued for several decades, especially since the introduction of optical fiber telecommunications. Several different designs have been proposed and prototypes implemented [1–13] with different degrees of success. There are three main criteria that determine the quality of a prototype and its proximity to commercialization or industrial applicability. These criteria consist of the following: isolation ratio, defined as the ratio between the optical power allowed to exit the device in the backward and forward directions, insertion loss, and footprint. Usually, the figure of merit for these devices is defined as the isolation ratio over insertion loss. But this figure of merit does not encompass the footprint criterion, which in magneto-optic isolator prototypes entails a reduction in size or elimination of the magnetizing element altogether [14].

Magneto-optic systems have been extensively explored because of the nonreciprocal character of the underlying phenomenon. This is a well-established optical isolator technology that is used in most commercial devices. Two main operating principles have been explored for on-chip magneto-optic isolators, Faraday rotation [14–17] and the nonreciprocal phase shift effect [11,13,18]. Other approaches have also been proposed and studied, such as dynamic nonreciprocity [19], optomechanically induced nonreciprocity, a nonmagnetic method, which addresses the elimination of the magnet [20], and nonlinear techniques [21,22]. The latter, however, do not provide isolation for arbitrary backward-propagating noise [23].

The purpose of the present communication is to report on the practical implementation and performance of an alternative concept in magneto-optic isolator technology, namely topological edge-state isolators in the optical regime. Topological edge-state phenomena have been proposed in recent years and investigated theoretically and experimentally [24–29]. They have been applied in the microwave regime to demonstrate unidirectional propagation in magneto-optical photonic crystals [29]. Here, we present a report on the experimental performance of Su-Shrieffer-Heeger (SSH)-type topological edge-state structures in the optical regime, fabricated in liquid-phase-epitaxy (LPE)-grown bismuth-substituted lutetium iron garnet films.

Zhou and co-workers have proposed a theoretical model based on a SSH topological construction similar to the one presented here, but of a nonlinear type [22]. There are important differences between the linear model implemented experimentally in our work and the nonlinear model proposed in Ref. [22]. Our system is not restricted to the high-power inputs needed to produce Kerr-like refractive index nonlinearities and does not rely on asymmetric power-coupling efficiencies in the forward and backward directions, as proposed in Ref. [22]. In addition, as demonstrated in Ref. [23], there is a class of small-amplitude waves for which nonlinear isolators based on Kerr or Kerr-like nonlinearities cannot provide optical isolation for arbitrary backward-propagating noise. That is not the case in our implementation.

Two of the authors of the present work have theoretically proposed and discussed a linear SSH

*mlevy@mtu.edu

topological isolator on a different materials system than reported here [30]. The present work produces an experimental realization, thus allowing the authors to provide a characterization of the actual performance of a SSH array in bismuth-substituted iron garnet films. The degree of isolation of the edge state from light launched into and propagating in the other array channels, as well as its insertion loss, are analyzed on the basis of experimental performance. Based on these experimental results, the present manuscript analyzes and proposes optical-isolator edge-state structures having significantly reduced footprints compared to previous designs and the means to implement the required on-chip magnetization.

It should be emphasized that the effort to realize industrially viable on-chip optical isolators for optical circuit integration, particularly at telecom wavelengths, has already spanned more than three decades. This vast international effort testifies to the importance of the miniaturization of these nonreciprocal devices for commercial applications. Most of this work has relied on the use of magneto-optic materials, such as rare-earth-substituted iron garnets and Faraday rotation or the nonreciprocal phase-shift effects. The reason for this is the intrinsic nonreciprocity of these magneto-optic effects. Steady progress has been made and continues to be made toward the implementation of viable integrated magneto-optic isolator devices competitive with bulk commercial isolators, not only in performance but also in production costs.

It should also be pointed out that a key rationale for the introduction of spatial-temporal modulation schemes as in Refs. [19,31] is the desire to eliminate the bulky magnetic biasing component in magneto-optic based optical isolators, particularly for on-chip integrated device purposes. Nevertheless, previous work by some of the authors of the present work has already demonstrated that it is possible to integrate the bias magnet on chip in a waveguide isolator [5] or to completely eliminate the magnetizing element in submillimeter Faraday rotators [14]. At the same time, progress is being made in the practical implementation of isolators based on modulation schemes, both in the optical [19] as well as in the microwave regimes [32,33]. Other models being proposed for the microwave regime include the use of electronic components [34,35] and ferroelectric materials [36,37].

The work reported here is the first partial implementation of an on-chip magneto-optic isolator based on the topological edge-state SSH model. These types of isolators have been predicted to deliver much higher isolation ratios, up to -50 dB at telecommunication wavelengths, than any other on-chip isolator device types [30]. This predicted isolation behavior arises from the existence of a topological edge state in the forward propagation direction and its destruction in the backward direction. The topological features of the SSH model are connected to the chiral symmetry of the system and they are the reason why the zero- or mid-gap mode still persists if the coupling coefficients of the fabricated structure deviate from the ideal design, as they do in our implementation. Numerical results by one of the authors, not presented here, have shown that a nontopological edge state formed by detuning the edge waveguide can also lead to isolation effects, but with two drawbacks: (1) Smaller isolation ratios; (2) More susceptibility to disorder. In this regard, our topological system provides a clear advantage.

The fact that our fabricated structure generates a topological edge state in one propagation direction is, in and of itself, not the reason why it functions as an optical isolator. Its performance as an isolator is not predicated on the unidirectional propagation of chiral edge states of the type induced in two-dimensional magneto-optic topological "insulator" photonic structures, such as that realized in Ref. [28] in the microwave regime. Rather, in our structure, it is the symmetry breaking (between the forward and backward propagating waves) induced by the presence of transverse magnetization through the nonreciprocal phase-shift effect that destroys the topological edge state in the backward propagation direction, and it is this that is responsible for the isolation functionality of our system.

Some of the most advanced work realized on waveguide magneto-optic isolators in the optical regime, based on years of excellent developmental work, have delivered -30 dB of isolation in Mach-Zehnder structures with 13 dB insertion loss [9] and -19.5 dB of isolation in ring resonators with 18.2 dB insertion loss [13]. The latter types are restricted to narrow bands of operation, which is not the case for SSH edge-mode isolators. Without the benefit of years of optimization work, this first implementation of SSH topological edge-state devices in a nonreciprocal system already shows power confinement in the edge channel relative to its farthermost channel as high as 29 dB, and average insertion losses of less than 2 dB in the edge channel vs total output power in the forward direction.

II. DESIGN AND OPERATING PRINCIPLES

This work proposes and implements a waveguide structure based on topological ideas for use in on-chip optical isolators. Topology deals with features that are not altered under certain continuous deformations of the object in question. In this particular case, the topologically protected feature consists of a waveguide-propagation mode that remains geometrically separate and isolated from other channels in the array. This waveguide mode is protected against fabrication errors in interchannel gaps (coupling constants) and channels widths (propagation constants).

The proposed device consists of a seven-waveguide-array SSH construction, as depicted in Fig. 1. This communication reports the experimental fabrication of the topological edge-state portion of the device and its performance as described below.

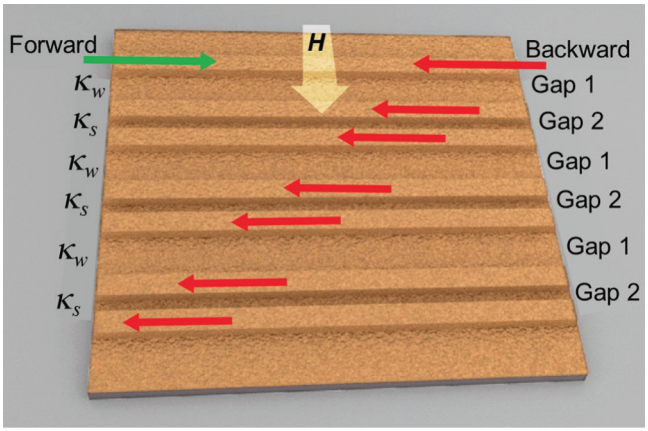

FIG. 1. Schematic of the SSH array, κ_w and κ_s are the alternating weak and strong coupling coefficients between the waveguides corresponding to wider and narrower gaps: gap1 and gap2, respectively. The direction of the magnetizing field on the edge channel is indicated.

SSH constructions create a topologically protected midgap edge state in the photonic band structure generated by the waveguide array [24–26,30], as detailed in the Appendix. SSH edge states form in coupled arrays with alternating coupling constants κ_s and κ_w, $\kappa_s > \kappa_w$, and an odd number of waveguide channels [30]. This construction gives rise to a topologically protected normal mode propagating on one edge in the array. The topologically protected state results from the alternating interwaveguide coupling constant and prevents the light from diverging into the bulk of the array. The ratio κ_w/κ_s determines the level of protection of the edge state against departures from uniformity in κ_s or κ_w across the array or in propagation constant in the individual array channels [24]. The nonreciprocal magneto-optic effect induces a change in propagation constants in the backward direction that destroys the edge state, as discussed theoretically in Ref. [30]. Our measurements show that this device delivers <2 dB of delocalization of optical power from the edge state, and more than 25 dB of extinction in the farthermost channel from the edge waveguide in the three arrays studied. Figure 1 schematically shows the beam propagation structure based on this principle.

The experimental results presented below report the edge-state selectivity corresponding to the power reaching the output channel in the forward direction when light is coupled to the edge-state channel vs other channels in the SHH array. Spreading of the power in other channels from the edge state can be minimized by engineering metallic optical absorbers as discussed in Ref. [30] without affecting the forward output power. LPE-grown iron garnet core waveguides on lattice-matched garnet substrates are used to fabricate the devices reported in this communication. These generally generate lower power absorption losses than found in other fabrication techniques [1,2,13,38–41]. At the same time, they do not deliver as large a nonreciprocal phase shift [42] as sputter- or pulsed-laser-deposited iron garnets on silicon waveguides [43] as shown in the Appendix for two reasons. First, the level of bismuth or cerium substitution needed to enhance the magneto-optic gyrotropy over that of pure yttrium iron garnet (YIG) is lower in LPE-grown films due to substitutional saturation conditions in the growth melt. Second, having the iron garnet as a cover layer on high-index core films, such as silicon, generates a larger nonreciprocal phase shift effect (NRPS) effect as a result of magneto-optic helicity biasing in the evanescent tail. Conclusions about the performance of higher magneto-optic gyrotropy materials are also drawn from our experimental data.

The footprint of the SSH arrays depends on the strength of the magneto-optic gyrotropy parameter in the bismuth-substituted iron garnet film, and on the κ_w/κ_s ratio in the SSH structure. Nonreciprocal power transfer between the two channels in opposite propagation directions is a function of the corresponding nonreciprocal phase shift. A stronger coupling constant between the channels requires a stronger gyrotropy parameter for smaller footprints, full power transfer in the backward direction, and optical revival in the edge-state channel in forward propagation. These gyrotropy values range from approximately 0.0003 to 0.002 depending on the level of bismuth substitution in the iron garnet at a 1.55 μm wavelength. Higher values of approximately 0.008 are attainable in Ce-substituted iron garnets [13,38,39].

III. FABRICATION AND DEVICE SPECIFICATIONS

The topological edge-state waveguide arrays are fabricated on LPE-grown films of bismuth-substituted lutetium iron garnet film (Bi:LuIG) with composition $Bi_{0.7}Gd_{0.4}Lu_{1.9}Fe_{4.1}Ga_{0.9}O_{12}$ on (100) gadolinium gallium garnet (GGG). The iron garnet films are initially etched down to approximately 500 nm thickness from 2-μm-thick virgin films by wet etching in ortho-phosphoric acid at 150 °C. Electron-beam lithography is used to pattern 350-nm-thick positive electron-beam resist array masks. A 30-nm-thick gold layer is sputter deposited on top to avoid electron beam charging while writing on the insulating Bi:LuIG film. Eight-mm-long waveguides arrays are formed by the beam through multiple stitching at a writing field of $500 \times 500\ \mu m^2$. After the e-beam exposure, the thin gold layer is removed by wet etching in gold etchant and the exposed resist is developed in amyl acetate solution. These patterns are then transferred into the Bi:LuIG film by argon-ion-beam milling. The sample holder is rotated at 10 revolutions per minute (rpm) and cooled at 6 °C throughout the process for uniform etching while tilted at 75° to the ion beam to prevent redeposition on the side

TABLE I. Dimensions of waveguide (WG) widths and gaps in design and post-fabrication (post-fab).

	SSH array 1				SSH array 2				SSH array 3			
	Design		Post fab.		Design		Post fab.		Design		Post fab.	
WG no.	Width (μm)	Gaps (μm)	Width (μm)	Gaps (μm)	Width (μm)	Gaps (μm)	Width (μm)	Gaps (μm)	Width (μm)	Gaps (μm)	Width (μm)	Gaps (μm)
1	2		1.772		2		1.786		2		1.762	
		1		1.127		1.2		1.294		1.2		1.365
2	2		1.883		2		1.88		2		1.828	
		0.8		0.892		0.9		0.973		1		1.112
3	2		1.858		2		1.871		2		1.861	
		1		1.065		1.2		1.257		1.2		1.308
4	2		1.895		2		1.89		2		1.713	
		0.8		0.855		0.9		0.966		1		1.035
5	2		1.895		2		1.884		2		1.61	
		1		1.065		1.2		1.264		1.2		1.122
6	2		1.883		2		1.876		2		1.619	
		0.8		0.917		0.9		0.95		1		0.951
7	2		1.821		2		1.851		2		1.741	

walls of the resist structure. After 80-min milling, 225-nm waveguide ridges are obtained. The remaining resist coating is removed by soaking in N-methyl pyrrolidine (NMP) heated to 80 °C for half an hour.

The design and fabricated device dimensions are tabulated below in Table I for each of the arrays studied here. The ridge waveguides are 500 nm thick, with ridge steps of 250- and 250-nm-slab thickness. Ridge widths are designed for 2 μm, but actual fabricated widths range as shown in Table I. Scanning-electron micrographs (SEM) images of the input and output regions (a) and the middle coupling region (b) are shown in Fig. 2 for one of the arrays. Ancillary input and output channels [Fig. 2(a)] are fabricated to facilitate separate coupling and probing of each.

The fabricated channel-waveguide widths depart from the 2-μm design width. Deviations from design are nearly uniform throughout the arrays and are less than 100 nm. As we shall see from the performance results below, these departures from device specification do not destroy the topological edge state.

IV. POWER SELECTIVITY AND INSERTION LOSS PERFORMANCE

SSH array structures concentrate most of the propagating optical power in the edge channel corresponding to the topological edge state when light is coupled into that channel. When light is input into any of the other channels, they distribute power throughout the whole array, even when coupled into the farthermost channel on the opposite end of the topological structure.

This operation is verified in Fig. 3, which shows IR CCD camera intensity-profile images of the power from the seven output channels captured by the camera for different input locations. Each row in the insets corresponds to the output signal from an input into successive waveguides, with the topological edge-state output at the top of each panel. Images for the three arrays are displayed for TM and TE mode inputs, showing that all the arrays perform as topological edge-state structures for both waveguide modes. Experimentally measured intensity profiles for the topological edge state are also presented, together with

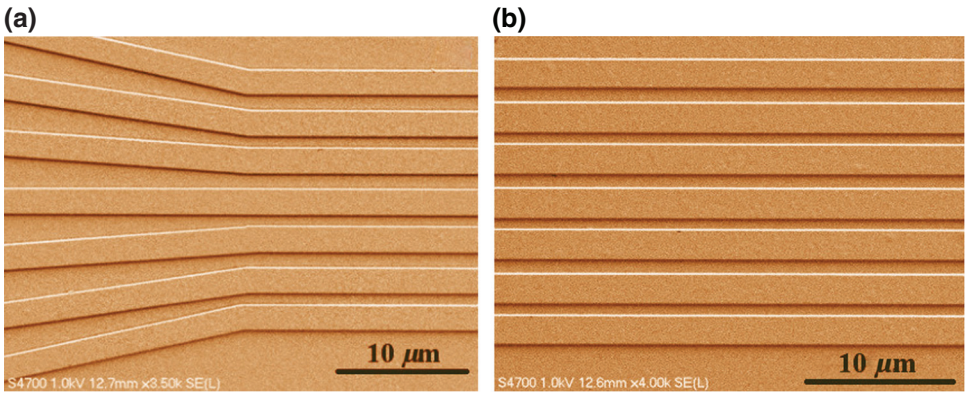

FIG. 2. SEM images of a fabricated SSH array: (a) Input and output regions and (b) coupling region.

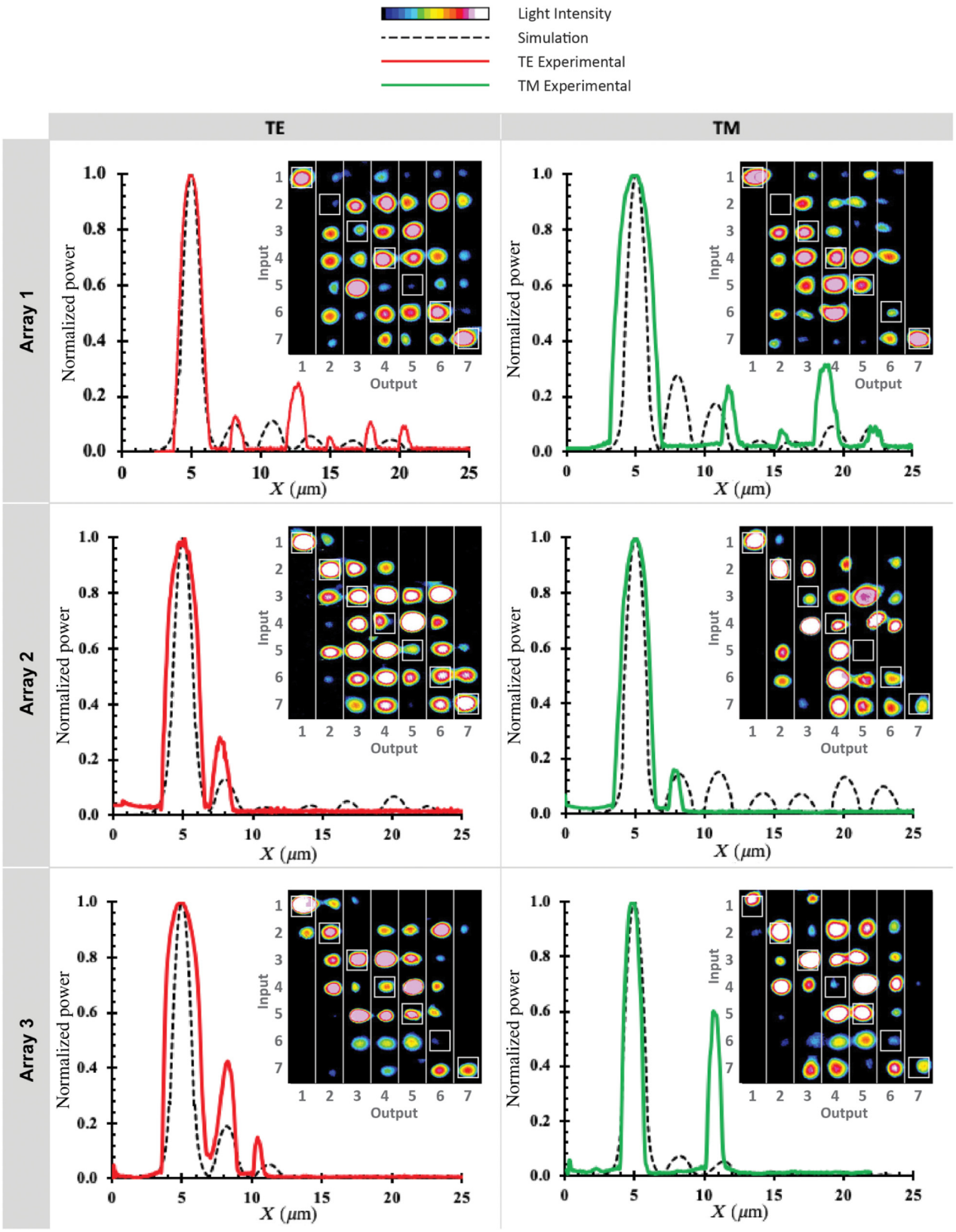

FIG. 3. Simulation vs experimental normalized output power of edge states for three SSH arrays under study for TE and TM modes. The insets show IR CCD camera intensity-profile images of the respective array outputs when input light is coupled into waveguide 1 (top row profile, edge-state channel) up to waveguide 7 (bottom row profile). The white squares in each inset denote the corresponding input waveguide. Differences between experimental and simulated edge-state intensity profiles are ascribed to the fabricated device's dimension deviations from design.

their corresponding beam-propagation simulation (BPM) profiles, showing good agreement.

The BPM simulations confirm that the fabricated arrays perform as expected for topological edge-state structures. Light coupled into the edge waveguide remains confined to the edge, whereas light input into other channels produces beams that diverge throughout the array, as shown in Fig. 3.

BPM-simulated edge-state propagation for the three SSH designs are also shown in Figs. 4(a)–4(c). Each simulated waveguide structure is 2 μm wide and 500 nm in ridge height with 250 nm of slab, in agreement with the design, but differing somewhat from the actual fabricated arrays. The coupling coefficients in the SHH model are controlled by the separation between the waveguides. The three SSH arrays studied here are defined by the two different alternating gaps (a) 1 and 0.8 μm in array 1, (b) 1.2 and 0.9 μm in array 2, and (c) 1.2 and 1 μm in array 3. The strongest coupling coefficient values in the above arrays are 13.8, 10.4, and 8.0 cm^{-1}, respectively.

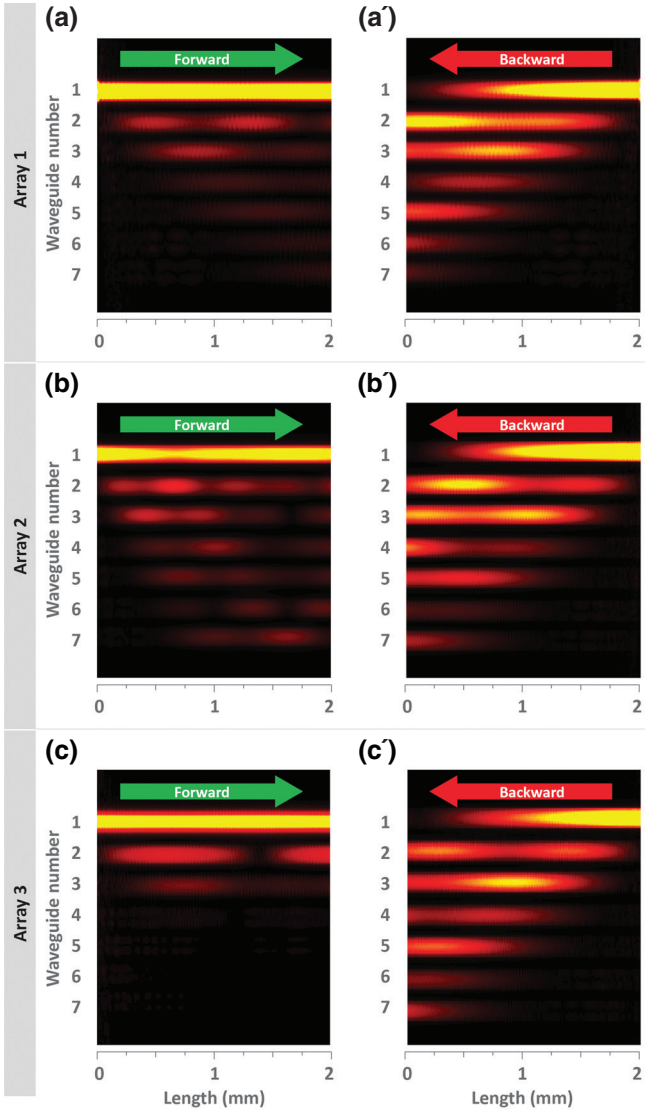

FIG. 4. BPM-simulated topological edge-state propagation in three SSH model waveguide arrays for forward and backward propagation directions: (a), (b), and (c) forward propagation; (a′), (b′), and (c′) backward propagation for the three arrays, respectively.

Isolator-function operation is simulated in Figs. 4(a′)–4(c′) exhibiting almost complete power extinction in the edge waveguide for nonreciprocal phase shifts $\Delta\beta^{nr}$ 26.8, 24.1, and 18.5 cm^{-1}, respectively, in the corresponding edge waveguide. This approximate extinction occurs after 2.5- to 4-mm propagation lengths.

The performance of the topological edge state is measured by butt-coupling 1.55-μm wavelength light from a lensed optical fiber into polished facets of the topological edge waveguide. For analytical purposes, light from the fiber is also coupled into each of the other channels for both TE and TM input modes. IR CCD camera images are also taken of the intensity distribution profiles as shown in Fig. 3 insets. These images evince how the light remains at the topological edge or gets dispersed into the other channels, depending on the coupling and on each particular array.

In order to characterize the performance of the fabricated structures, the power coming out of the edge-state channel (waveguide number 1 in Fig. 3) is compared to the incident power, as defined below, for light coupled into channels one to seven. This actually measures the degree of localization of the edge-state light when coupled to the edge-state channel vs any other channel as input.

Incident power is defined as the sum of the powers coming out of all of the channels in the array. This definition of incident power folds out mode conversion and Fresnel losses at the input facet. It also does not account for optical absorption and scattering losses in the array channels. This configuration also allows us to define insertion loss as the ratio of the light emerging out of topological edge channel divided by the total incident power, as defined above.

Table II tabulates these results for both TE and TM modes of input excitation. It also tabulates the power emerging from the topological edge channel (waveguide 1) and the opposite outermost channel (waveguide 7) when light is coupled into waveguide 1, and the power in the edge waveguide 1 when light is coupled into the other channels, 2 to 7. Less than 1 dB of power is distributed among other waveguides in all three arrays in TE modes resulting in up to 28.6 dB of extinction in the outermost channel 7 when the light is mainly localized in the edge mode. In TM mode, the delocalization of the edge mode is below 3 dB in two of the arrays. In array 3, the higher delocalization value (5.3 dB) is attributed to damage to the device during the fabrication process that also results in relatively lower power transmission compared to other

TABLE II. Optical power measurement on three fabricated SSH arrays for both TM and TE modes.

TE mode									
	Measured power, array 1			Measured power, array 2			Measured power, array 3		
Fiber coupled WG no.	Total (μW)	Edge WG1 (dB)	WG7 (dB)	Total (μW)	Edge WG1 (dB)	WG7 (dB)	Total (μW)	Edge WG1 (dB)	WG7 (dB)
1	1.003	−1.0	−23.0	3.603	−0.1	−25.6	1.360	−0.7	−28.6
2	3.487	−15.1		5.904	−15.0		0.566	−6.9	
3	2.254	−10.8		4.516	−18.1		1.217	−15.9	
4	4.942	−12.1		8.453	−28.1		1.090	−21.7	
5	3.607	−11.6		5.355	−21.7		1.223	−22.7	
6	3.577	−17.8		5.513	−27.6		0.029	−21.1	
7	3.137	−18.6		2.590	−17.1		0.655	−19.1	
TM mode									
	Measure power, array 1			Measured power, array 2			Measured power, array 3		
Fiber coupled WG no.	Total (μW)	Edge WG (dB)	WG7 (dB)	Total (μW)	Edge WG (dB)	WG7 (dB)	Total (μW)	Edge WG (dB)	WG7 (dB)
1	3.776	−1.2	−21.0	1.228	−2.9	−22.0	0.932	−5.3	−25.8
2	2.491	−13.9		1.033	−13.5		0.364	−1.6	
3	2.442	−12.2		7.673	−27.2		1.010	−13.2	
4	10.008	−16.1		5.399	−15.2		1.095	−14.0	
5	12.593	−17.3		3.286	−24.1		0.505	−11.3	
6	4.166	−14.3		1.823	−22.4		0.025	−0.2	
7	0.639	−11.9		0.395	−13.3		0.078	−23.6	

arrays in the TM mode. Power extinction in the outermost channel is measured as 25.8 dB in this case.

Noticeably, there is very low power coming out of the edge waveguide 1 in the cases when the input is launched from all other waveguides. This can also be seen clearly from the second to seventh row profiles of the outputs in the insets to Fig. 3. The experimentally measured edge-mode profiles closely resemble their respective BPM-intensity profile for both TE and TM modes, also shown in the same figure. This distinctly differentiates topological edge modes from the nontopological modes.

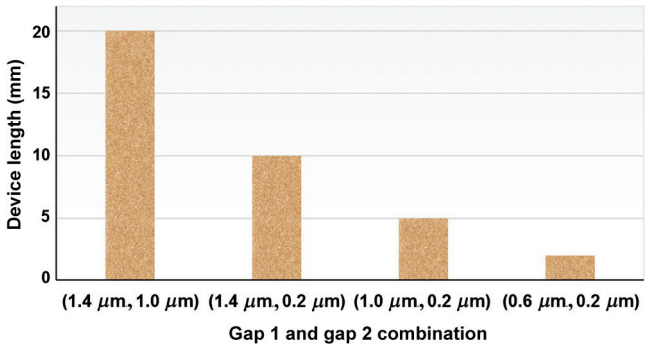

FIG. 5. Device length for different coupling coefficients as controlled by separation between waveguides: gap1 and gap2 corresponding to the weaker and stronger coupling coefficients κ_w and κ_s, respectively.

The fabricated SSH arrays studied here (coupling region) are 7 mm long. However, the device length can be shortened by increasing the coupling coefficients, thus reducing the distance between the optical channels. Devices can be made submillimeter in length by reducing channel gaps to the shortest limit presently allowable by fabrication techniques, below 100 nm via e beam lithography and plasma etching. The preservation of power in the edge-state channel is highest when the contrast between the values of the coupling coefficients is greatest. Thus there is a trade-off between device length and the localization of edge-mode power. As shown in Fig. 5, the device length shortens from 20 to 10 mm when the interchannel gap corresponding to κ_s is reduced from 1 μm to 200 nm while keeping the other gap at 1.4 μm. The device length gets further reduced to 2 mm when the gap corresponding to κ_w is 0.6 μm.

V. CHALLENGES

Full implementation of an optical isolator of this type requires $\Delta\beta^{nr} \geq \kappa_s$. In our case, $\Delta\beta^{nr} = 4\ \mathrm{cm}^{-1}$ while κ_s is 26.8 cm^{-1}, 24.1 cm^{-1}, and 18.5 cm^{-1} for the three arrays studied here. Therefore, the above condition is not

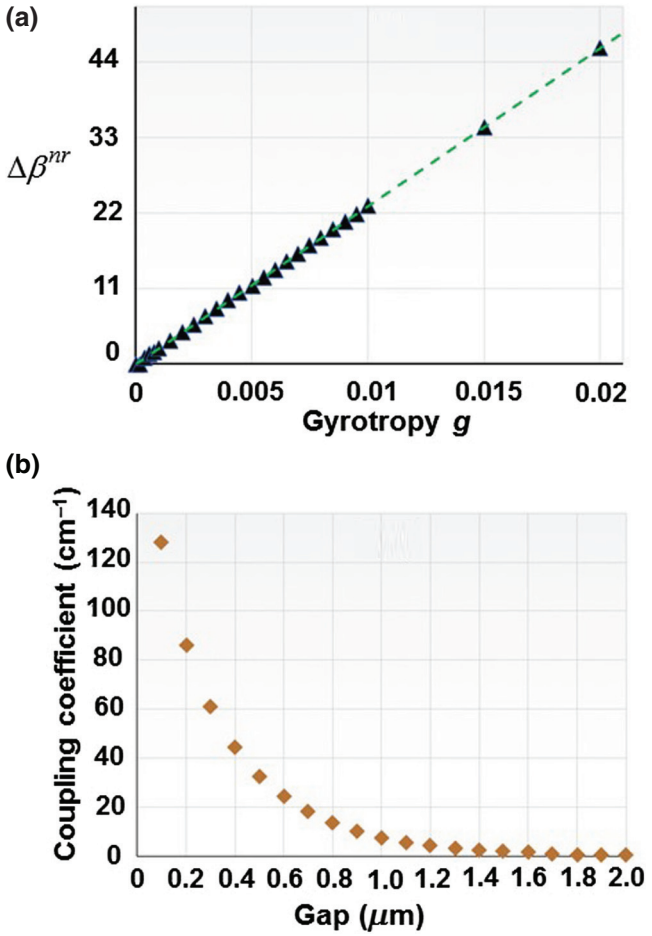

FIG. 6. (a) Value of the magnetic gyrotropy needed to meet the condition $\Delta\beta^{nr} \geq \kappa_s$for delocalization (isolation function) to occur in the backward direction. (b) Coupling coefficient variation with separation between Bi:LuIG channels.

satisfied. To incorporate this $\Delta\beta^{nr}$ into a working optical isolator, the interchannel gap for κ_s would have to be $\geq$1.3 μm, requiring a device longer than 20 mm.

Figure 6 plots coupling coefficient as a function of channel separation for the material parameters used in this work. Figure 6(a) gives the gyrotropy parameter of the magneto-optic film needed to produce the nonreciprocal phase shift required to delocalize the light from the edge waveguide for backward propagating light. Reducing the coupling coefficient through an increase in interchannel separation increases the device length to >20 mm for a gap greater than 1.3 μm.

Conversely, one could attain larger values of $\Delta\beta^{nr}$ with Ce-substituted iron garnets [39] or by utilizing double layers of iron garnets [42] on GGG substrates with $\Delta\beta^{nr}$ as high as 40 cm^{-1}. With Ce-YIG covers on SOI waveguides, $\Delta\beta^{nr}$ values become as large as 70 cm^{-1} [43] and device footprints of approximately 1 mm are feasible.

However, magnetic-garnet films deposited on SOI waveguides suffer from higher propagation losses compared to LPE-grown garnet core waveguides. Reducing the isolator footprint to the smallest levels allowed by present fabrication technologies (sub-100-nm gaps) would produce footprints of approximately 1 mm. This requires iron garnet materials be developed with correspondingly higher nonreciprocal phase shifts. For example, using 100-nm gaps for stronger coupling requires $\Delta\beta^{nr} \sim 128$ cm^{-1}, corresponding to gyrotropy parameters of 0.05 for the magneto-optic film.

Topological edge-state devices, such as those discussed here, require the magnetization of the garnet on the edge channel opposite to that of the rest of the array [43]. This calls for localized magnetic fields and relatively large magnetic field gradients near edge [43]. Such conditions could be implemented by depositing approximately $2-\mu$m$-$ thick samarium-cobalt films with an intermediate buffer layer on top of the array [5]. Other options entail thin current-carrying conducting wires, as thin as 20 or 30 μm, and cannot withstand high enough currents to achieve the required saturation fields unless they are superconducting. Tests in our laboratory with $20-\mu$m-thin gold wires are thus limited to currents of 0.5 A. Alternative electromagnet designs to achieve an in-plane saturation field with a current as small as 0.25 A have been discussed by other authors [41].

VI. CONCLUSIONS

We experimentally measure and analyze the degree of localization of edge modes in SSH arrays designed for LPE-grown Bi:LuIG films on GGG substrates. A high degree of optical localization is observed for both TE and TM input excitations with less than 2% of optical input power spread in the remaining six waveguide channels out of seven channels in the arrays fabricated. The edge-states mode is clearly distinct from the other array modes favoring isolation of the edge channel, which is the motivating factor toward realizing this effect in a fullfledged optical isolator.The device length can be reduced to approximately 1 mm via optimization of the waveguide film-core configuration to yield higher nonreciprocal phase shifts than implemented in this work.

APPENDIX

The type of topological structure that we consider here, known as SSH, has been investigated before in polymer science, and was shown to produce topologically protected localized states [44]. In the optical regime, a similar topologically protected state can be achieved via the interleaving of coupling constants between optical channels in a waveguide array, as shown in Fig. 1 [30].

Such a multichannel optical array exhibits several normal or array modes, with different propagation constants and optical power distributions across the array. The insertion of alternating coupling constants between the optical

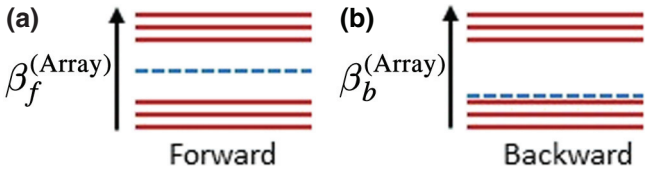

FIG. 7. Schematic depiction of array-mode propagation constants showing (a) the topologically protected propagating constant in the forward direction and (b) the propagation constant of the otherwise mid-gap state is now pushed toward the lower band. As a result, the corresponding mode is delocalized in the backward propagation direction due to the NRPS effect of the guided mode in the magnetic garnet film.

channels in the SSH model opens up a band gap between propagation constants of the array, as depicted schematically in Fig. 7. If the array consists of an odd number of channels and is terminated in a waveguide weakly coupled to its nearest neighbor, the edge waveguide, then a propagation mode is located in the middle of the band gap, Fig. 7(a), and is protected against fabrication errors that can shift it away from the gap center. Light coupled into this channel remains confined to it as it propagates in the forward direction.

Optical isolator technology makes extensive use of magneto-optic effects because these can be applied to induce highly efficient transmission in the forward propagation direction and to block the passage of light in the opposite direction. In our case, this type of nonreciprocity is implemented through the transverse magnetization of the topologically protected edge-waveguide channel. Light propagating in one direction (the forward direction) remains confined to this channel. However, light propagating in the opposite (backward) direction has its propagation constant shifted by the magneto-optic effect, as shown in Fig. 7(b). This nonreciprocal propagation constant shift is known as the nonreciprocal-phase-shift-effect (NRPS) and has been applied to fabricate interferometric optical isolators of the Mach-Zehnder type [45]. In the SSH structure proposed here, the NRPS delocalizes the edge mode by shifting its propagation constant out of the band gap, inducing coupling with the other array modes.

Within the formalism of coupled mode theory, the system is described by

$$i\frac{d\vec{a}_{f,b}}{dz} = H_{f,b}\vec{a}_{f,b},$$

where

$$H_{f,b} = \begin{pmatrix} \beta_{f,b} & \kappa_w & 0 & \dots & 0 \\ \kappa_w & \beta & \kappa_s & \dots & 0 \\ \dots & \dots & \dots & \dots & \dots \\ 0 & 0 & \dots & \beta & \kappa_s \\ 0 & 0 & \dots & \kappa_s & \beta \end{pmatrix}. \tag{A1}$$

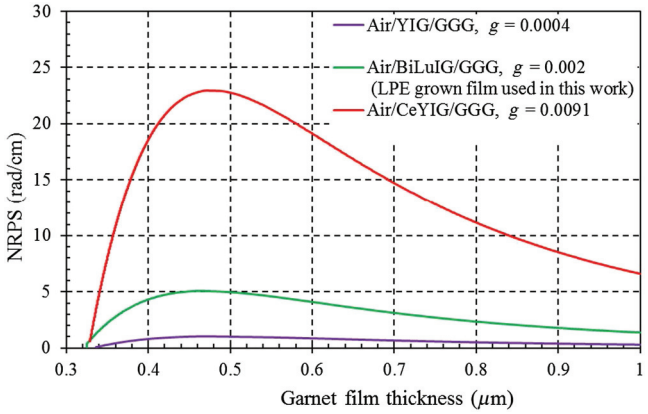

FIG. 8. NRPS variation with garnet film thickness on air/garnet/GGG layers with parameters at 1550-nm wavelength, GGG substrate refractive index 1.93, and film index 2.22.

The components of the vector $\vec{a} = [a_1, a_2, \dots, a_N]^T$ in Eq. (A1) stand for the optical-field amplitudes in the individual waveguide channels of the array, with N being the total number of channels. z is the propagation distance, and the weak and strong values of the coupling coefficients are represented by $\kappa_{w,s}$. The superscript T indicates matrix transpose, with the first waveguide exhibiting different propagation constants $\beta_{f,b}$ in the forward and backward propagation directions.

This difference is induced by transverse magnetization of the first channel, whereas all the other waveguides have propagation constant β matching that of β_f in the forward direction. It is assumed that the other channels are either not magnetized or are oppositely magnetized to the edge channel. In the latter case, the lateral dimensions of the first waveguide can be adjusted so that $\beta_f = \beta$. Their propagation constants are thus matched in the forward propagation direction and differ in the backward direction.

The array-mode propagation constants are found by solving the eigenvalue problem in Eq. (A2).

$$H_{f,b} = \begin{pmatrix} \beta_{f,b} & \kappa_w & 0 & \dots & 0 \\ \kappa_w & \beta & \kappa_s & \dots & 0 \\ \dots & \dots & \dots & \dots & \dots \\ 0 & 0 & \dots & \beta & \kappa_s \\ 0 & 0 & \dots & \kappa_s & \beta \end{pmatrix} \vec{a}_{f,b} = \beta_{f,b}^{(\mathrm{Array})}\vec{a}_{f,b}. \tag{A2}$$

Figure 8 plots the value of the NRPS, $\beta_f - \beta_b$, as a function of film thickness. Different values of the gyrotropy parameter g are obtained by varying the bismuth substitution level in the iron garnet crystal.

ACKNOWLEDGMENTS

D.K. and M.L. acknowledge support from the Henes Center for Quantum Phenomena. The authors thank K.

Roberts for help with e beam lithography at the Minnesota Nano Center and C. Kendrick for helpful discussions.

[1] H. Dötsch, N. Bahlmann, O. Zhuromskyy, M. Hammer, L. Wilkens, R. Gerhardt, P. Hertel, and A. F. Popkov, Applications of magneto-optical waveguides in integrated optics: Review, J. Opt. Soc. Am. B **22**, 240 (2005).

[2] P. Dulal, A. D. Block, T. E. Gage, H. A. Haldren, S.-Y. Sung, D. C. Hutchings, and B. J. H. Stadler, Optimized magneto-optical isolator designs inspired by seedlayer-free terbium iron garnets with opposite chirality, ACS Photonics **3**, 1818 (2016).

[3] R. El-Ganainy, A. Eisfeld, M. Levy, and D. N. Christodoulides, On-chip non-reciprocal optical devices based on quantum inspired photonic lattices, Appl. Phys. Lett. **103**, 161105 (2013).

[4] Y. Hideki, I. Shun, and U. Yuki, Interferometric optical isolator with Air/Si/magnetic-garnet waveguide operated in unidirectional magnetic field, Jpn. J. Appl. Phys. **49**, 058002 (2010).

[5] M. Levy, R. M. Osgood, Jr., H. Hegde, F. J. Cadieu, R. Wolfe, and V. J. Fratello, Integrated optical isolators with sputter-deposited thin-film magnets, IEEE Photonics Technol. Lett. **8**, 903 (1996).

[6] Y. Shoji, M. Ito, Y. Shirato, and T. Mizumoto, MZI optical isolator with Si-wire waveguides by surface-activated direct bonding, Opt. Express **20**, 18440 (2012).

[7] K. Shui, L. Nie, Y. Zhang, B. Peng, J. Xie, L. Deng, and L. Bi, Design of a compact waveguide optical isolator based on multimode interferometers using magneto-optical oxide thin films grown on silicon-on-insulator substrates, Opt. Express **24**, 12856 (2016).

[8] Y. Sobu, Y. Shoji, K. Sakurai, and T. Mizumoto, GaInAsP/InP MZI waveguide optical isolator integrated with spot size converter, Opt. Express **21**, 15373 (2013).

[9] B. J. H. Stadler and T. Mizumoto, Integrated magneto-optical materials and isolators: A review, IEEE Photonics J. **6**, 1 (2014).

[10] M.-C. Tien, T. Mizumoto, P. Pintus, H. Kromer, and J. E. Bowers, Silicon ring isolators with bonded nonreciprocal magneto-optic garnets, Opt. Express **19**, 11740 (2011).

[11] C. Zhang, P. Dulal, B. J. H. Stadler, and D. C. Hutchings, Monolithically-integrated TE-mode 1D silicon-on-insulator isolators using seedlayer-free garnet, Sci. Rep. **7**, 5820 (2017).

[12] P. Pintus, D. Huang, C. Zhang, Y. Shoji, T. Mizumoto, and J. E. Bowers, Microring-based optical isolator and circulator with integrated electromagnet for silicon photonics, J. Lightwave Technol. **35**, 1429 (2017).

[13] L. Bi, J. Hu, P. Jiang, D. H. Kim, G. F. Dionne, L. C. Kimerling, and C. A. Ross, On-chip optical isolation in monolithically integrated non-reciprocal optical resonators, Nat. Photonics **5**, 758 (2011).

[14] D. Karki, V. Stenger, A. Pollick, and M. Levy, Thin-film magnetless Faraday rotators for compact heterogeneous integrated optical isolators, J. Appl. Phys. **121**, 233101 (2017).

[15] K. Shiraishi, F. Tajima, and S. Kawakami, Compact Faraday rotator for an optical isolator using magnets arranged with alternating polarities, Opt. Lett. **11**, 82 (1986).

[16] L. Sun, S. Jiang, J. D. Zuegel, and J. R. Marciante, All-fiber optical isolator based on Faraday rotation in highly terbium-doped fiber, Opt. Lett. **35**, 706 (2010).

[17] M. Shalaby, M. Peccianti, Y. Ozturk, and R. Morandotti, A magnetic non-reciprocal isolator for broadband terahertz operation, Nat. Commun. **4**, 1558 (2013).

[18] E. Ishida, K. Miura, Y. Shoji, H. Yokoi, T. Mizumoto, N. Nishiyama, and S. Arai, Amorphous-Si waveguide on a garnet magneto-optical isolator with a TE mode nonreciprocal phase shift, Opt. Express **25**, 452 (2017).

[19] H. Lira, Z. Yu, S. Fan, and M. Lipson, Electrically Driven Nonreciprocity Induced by Interband Photonic Transition on a Silicon Chip, Phys. Rev. Lett. **109**, 033901 (2012).

[20] Z. Shen, Y.-L. Zhang, Y. Chen, C.-L. Zou, Y.-F. Xiao, X.-B. Zou, F.-W. Sun, G.-C. Guo, and C.-H. Dong, Experimental realization of optomechanically induced non-reciprocity, Nat. Photonics **10**, 657 (2016).

[21] D. L. Sounas, J. Soric, and A. Alù, Broadband passive isolators based on coupled nonlinear resonances, Nat. Electron. **1**, 113 (2018).

[22] X. Zhou, Y. Wang, D. Leykam, and Y. D. Chong, Optical isolation with nonlinear topological photonics, New J. Phys. **9**, 095002 (2017).

[23] Y. Shi, Z. Yu, and S. Fan, Limitations of nonlinear optical isolators due to dynamic reciprocity, Nat. Photonics **9**, 388 (2015).

[24] A. Blanco-Redondo, I. Andonegui, M. J. Collins, G. Harari, Y. Lumer, M. C. Rechtsman, B. J. Eggleton, and M. Segev, Topological Optical Waveguiding in Silicon and the Transition Between Topological and Trivial Defect States, Phys. Rev. Lett. **116**, 163901 (2016).

[25] Y. E. Kraus, Y. Lahini, Z. Ringel, M. Verbin, and O. Zilberberg, Topological States and Adiabatic Pumping in Quasicrystals, Phys. Rev. Lett. **109**, 106402 (2012).

[26] E. J. Meier, F. A. An, and B. Gadway, Observation of the topological soliton state in the Su-Schrieffer-Heeger model, Nat. Commun. **7**, 13986 (2016).

[27] H. Schomerus, Topologically protected midgap states in complex photonic lattices, Opt. Lett. **38**, 1912 (2013).

[28] Z. Wang, Y. Chong, J. D. Joannopoulos, and M. Soljacic, Observation of unidirectional backscattering-immune topological electromagnetic states, Nature **461**, 772 (2009).

[29] Z. Wang, Y. D. Chong, J. D. Joannopoulos, and M. Soljacic, Reflection-Free One-Way Edge Modes in a Gyromagnetic Photonic Crystal, Phys. Rev. Lett. **100**, 013905 (2008).

[30] R. El-Ganainy and M. Levy, Optical isolation in topological-edge-state photonic arrays, Opt. Lett. **40**, 5275 (2015).

[31] Z. Yu and S. Fan, Complete optical isolation created by indirect interband photonic transitions, Nat. Photonics **3**, 91 (2009).

[32] S. Taravati, Giant Linear Nonreciprocity, Zero Reflection, and Zero Band Gap in Equilibrated Space-Time-Varying Media, Phys. Rev. Appl. **9**, 064012 (2018).

[33] S. Taravati, N. Chamanara, and C. Caloz, Nonreciprocal electromagnetic scattering from a periodically space-time modulated slab and application to a quasisonic isolator, Phys. Rev. B **96**, 165144 (2017).

[34] Z. Wang, Z. Wang, J. Wang, B. Zhang, J. Huangfu, J. D. Joannopoulos, M. Soljai, and L. Rana, Gyrotropic response in the absence of a bias field, Proc. Natl. Acad. Sci. U.S.A. **109**, 13194 (2012).

[35] S. Taravati, B. A. Khan, S. Gupta, K. Achouri, and C. Caloz, Nonreciprocal nongyrotropic magnetless metasurface, IEEE Trans. Antennas Propagat. **65**, 3589 (2017).

[36] S. Capraro, T. Rouiller, M. L. Berre, J.-P. Chatelon, B. Bayard, D. Barbier, and J. J. Rousseau, Feasibility of an integrated self biased coplanar isolator with barium ferrite films, IEEE Trans. Compon. Packag. Technol. **30**, 411 (2007).

[37] G. N. Jawad, C. I. Duff, and R. Sloan, A millimeter-wave gyroelectric waveguide isolator, IEEE Trans. Microw. Theory Tech. **65**, 1249 (2017).

[38] M. C. Onbasli, L. Beran, M. Zahradník, M. Kučera, R. Antoš, J. Mistrík, G. F. Dionne, M. Veis, and C. A. Ross, Optical and magneto-optical behavior of Cerium Yttrium Iron Garnet thin films at wavelengths of 200–1770 nm, Sci. Rep. **6**, 23640 (2016).

[39] M. Gomi, H. Furuyama, and M. Abe, Strong magneto-optical enhancement in highly Ce-substituted iron garnet films prepared by sputtering, J. Appl. Phys. **70**, 7065 (1991).

[40] Xin Zhou, You Wang, Daniel Leykam, and Y. D. Chong, Optical isolation with nonlinear topological photonics, New J. Phys. **19**, 095002 (2017).

[41] D. Huang, P. Pintus, C. Zhang, Y. Shoji, T. Mizumoto, and J. E. Bowers, Electrically driven and thermally tunable integrated optical isolators for silicon photonics, IEEE J. Sel. Top. Quantum Electron. **22**, 271 (2016).

[42] M. Wallenhorst, M. Niemöller, H. Dötsch, P. Hertel, R. Gerhardt, and B. Gather, Enhancement of the nonreciprocal magneto-optic effect of TM modes using iron garnet double layers with opposite Faraday rotation, J. Appl. Phys. **77**, 2902 (1995).

[43] H. Yokoi, Y. Shoji, and T. Mizumoto, Calculation of nonreciprocal phase shift in magnetooptic waveguide with Si guiding layer, Jpn. J. Appl. Phys. **43**, 5871 (2004).

[44] W. P. Su, J. R. Schrieffer, and A. J. Heeger, Soliton excitations in polyacetylene, Phys. Rev. B **22**, 2099 (1980).

[45] J. Fujita, M. Levy, R. M. Osgood, Jr., L. Wilkens, and H. Dötsch, Waveguide optical isolator based on Mach-Zehnder interferometer, Appl. Phys. Lett. **76**, 2158 (2000).